



Electron doping of a double-perovskite flat-band system

Lun Jin^{a,1} 📵, Nicodemos Varnava^{b,c}, Danrui Ni^a, Xin Gui^a, Xianghan Xu^a, Yuanfeng Xu^d, B. Andrei Bernevig^{c,d,e}, and Robert J. Cava^{a,1}

Contributed by Robert J. Cava; received November 11, 2022; accepted January 17, 2023; reviewed by Shuai Dong and Peter Schiffer

Electronic structure calculations indicate that the Sr₂FeSbO₆ double perovskite has a flatband set just above the Fermi level that includes contributions from ordinary subbands with weak kinetic electron hopping plus a flat subband that can be attributed to the lattice geometry and orbital interference. To place the Fermi energy in that flat band, electron-doped samples with formulas $Sr_{2-x}La_xFeSbO_6$ (0 $\leq x \leq$ 0.3) were synthesized, and their magnetism and ambient temperature crystal structures were determined by high-resolution synchrotron X-ray powder diffraction. All materials appear to display an antiferromagnetic-like maximum in the magnetic susceptibility, but the dominant spin coupling evolves from antiferromagnetic to ferromagnetic on electron doping. Which of the three subbands or combinations is responsible for the behavior has not been determined.

cation-ordered double perovskites | electron-doping | flat-band materials | X-ray powder diffraction | magnetism

Flat-band electronic materials have been a keen research topic in theoretical materials physics due to their potential for hosting strongly correlated electrons and hence exotic physical phenomena. However, related experiments are mostly limited to engineered materials, such as a moiré system (the electron density is necessarily low due to the large unit cell), rather than naturally occurring three-dimensional stoichiometric crystalline materials which have a potential for physical properties associated with high electron density. Complex metal oxides, as a vital component of stoichiometric crystalline materials, have been of enduring interest in a wide range of disciplines, as they can exhibit physical and chemical properties that are in large part determined by their crystal structures and electron count (1-5). The perovskite family, as one of the largest structural types in complex metal oxides, serves an important role in the material design area. B-site cation-ordered double perovskites, formula A₂BB'O₆, although more difficult to prepare than their cation-disordered analogs, can exhibit greater potential in engineering designed-for-purpose materials (6-8).

The double-perovskite Sr₂FeSbO₆, the basis of this study, has previously been reported and discussed regarding its crystal structure, with reports ranging from cubic (Fm-3m) to monoclinic $(P2_1/n \text{ and } I2/m)$ and further displaying a range of B-site cation mixing (about 80 to 90%) but without an in-depth discussion of its physical properties and band structures (9-14). Our previous electronic structure calculations (15) found it to exhibit a nearly flat band at energies just above the Fermi level through the entire Brillouin zone, due at least in part to the lattice geometry. Those calculations are augmented here, where we find that some of the orbitals contributing to the band arise from relatively poor Fe d-state orbital overlap (i.e., a signature of localized Fe ion states) but that a third arises from the lattice geometry and electron interference. This doped double perovskite is thus an unusual electronic system worthy of further study due to the potential electron occupancy of its topological flat band. Flat-band materials, especially those that have topological electronic flattened bands near or at the Fermi level, are prime candidates for hosting strongly correlated electrons (16) and can lead to exotic physical phenomena including magnetism, superconductivity, and the quantum anomalous Hall effect (17–25). Therefore, placing electrons into those bands, achieved here through the La-doping of Sr₂FeSbO₆, is worth investigating to determine whether unusual properties can be triggered.

In this study, the electronic structure of this material is further investigated, and to experimentally realize the flat band doping, La³⁺ is chosen to partially substitute for Sr²⁺ on the A-site of the Sr–Fe–Sb–O double perovskite (Sr_{2-x}La_xFeSbO₆), hence formally reducing some of the Fe³⁺ centers to Fe²⁺ centers in the B-site octahedra. The crystal structures of the undoped parent phase Sr₂FeSbO₆ and the newly synthesized La-doped materials are carefully examined by high-intensity high-resolution synchrotron powder X-ray diffraction. We find that a strong magnetic response is induced through the doping: the observations can be explained by both conventional and unconventional band occupancy. A delicate structure-property relationship is illustrated in the series of materials presented in this study, as evidenced by the modified properties upon introducing La³⁺

Significance

Flat-band electronic materials have been a keen research topic in theoretical materials physics due to their potential for hosting strongly correlated electrons and hence exotic physical phenomena. This study explores the electronic flat band (i.e., an electronic band that has minimal variation in energy over a significant portion of the Brillouin zone) located just above the Fermi level in Sr₂FeSbO₆. The origin of the flat band is theoretically determined, distinguishing it from ordinary bands, and to experimentally place the Fermi energy in that flat band, electron-doped samples are synthesized and analyzed, yielding some features that cannot be adequately described by classic physics in full. Our work shows that this doped double perovskite is an unusual electronic system worthy of further study.

Author affiliations: ^aDepartment of Chemistry, Princeton University, Princeton, NJ 08544; ^bDepartment of Physics & Astronomy, Rutgers University, Piscataway, NJ 08854; Donostia International Physics Center, 20018 Donostia-San Sebastian, Spain; ^dDepartment of Physics, Prince-ton University, Princeton, NJ 08544; and ^eIKERBASQUE, Basque Foundation for Science, 48009 Bilbao, Spain

Author contributions: L.J., N.V., B.A.B., and R.J.C. designed research; L.J., N.V., D.N., X.G., X.X., Y.X., B.A.B., and R.J.C. performed research; L.J., N.V., D.N., X.G., X.X., Y.X., B.A.B., and R.J.C. analyzed data; and L.J., N.V., B.A.B., and R.J.C.

Reviewers: S.D., Southeast University; and P.S., Yale

The authors declare no competing interest.

Copyright © 2023 the Author(s). Published by PNAS. This article is distributed under Creative Commons Attribution-NonCommercial-NoDerivatives License 4.0

¹To whom correspondence may be addressed. Email: ljin@princeton.edu or rcava@princeton.edu.

This article contains supporting information online at https://www.pnas.org/lookup/suppl/doi:10.1073/pnas. 2218997120/-/DCSupplemental.

Published February 14, 2023.

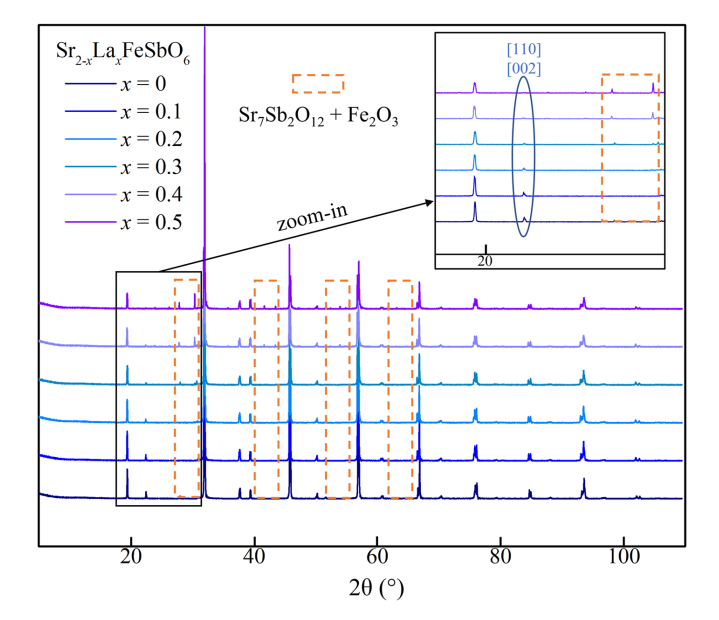


Fig. 1. Stacked lab X-ray powder diffraction patterns for compositions of the $Sr_{2-x}La_xFeSbO_6$ series, with orange boxes highlighting the growth of peaks representing the impurity phases $Sr_7Sb_2O_{12}$ and Fe_2O_3 . Inset: low angle area zoomed in.

dopant; changes in the crystal structure, magnetism, and electronic band occupancy of the parent compound are induced. Our experimental observations emphasize that it is critical to fully determine the crystal structures of materials prior to comprehensively understanding their physical properties. This study is a good example of how a characteristic of interest to physicists can be found in a class of materials of interest to solid-state chemists.

Results and Discussion

Structural Characterization. The stacked profile of lab pXRD data (Fig. 1) indicates that the maximum La^{3^+} -for- Sr^{2^+} substitution level is about 30% before the sample is no longer a single phase. Extremely small amounts of the impurity phases $\text{Sr}_7\text{Sb}_2\text{O}_{12}$ (PDF Card No. 00–034–1111 in ICDD) and Fe_2O_3 (PDF Card No. 00–013–0458 in ICDD) start to be observed in the x=0.3 pattern (in too trivial an amount to be reliably quantitatively characterized by structural refinement). These nonperovskite peaks grow in the x=0.4 and 0.5 patterns, while in contrast, the perovskite peaks (e.g., [110] and [002]) have shrunk significantly, as highlighted in the embedded plot of Fig. 1. This behavior indicates that the limit of the La solid solution is near x=0.3 for our synthetic conditions.

The ambient temperature crystal structure of the undoped parent phase Sr₂FeSbO₆ has been reported in the literature several times, but the symmetries range from cubic (Fm-3m) to monoclinic ($P2_1/n$ and I2/m) with a small distribution in the degree of B-site cation ordering (9-14). In our laboratory pXRD data, multiple weak reflections are clearly observed in addition to the strong peaks that can be indexed by a cubic unit cell (space group Fm-3m), and thus, the symmetry of the unit cell is not cubic. Both monoclinic space groups mentioned above $(P2_1/n \text{ and } I2/m)$ were refined against lab pXRD data and converged smoothly to give essentially undistinguishable agreement parameters. Although neutron and lab X-ray powder diffraction data of the undoped parent phase Sr₂FeSbO₆ have been reported, high-intensity high-resolution synchrotron X-ray powder diffraction (SXRD), which is capable of the observation of weak reflections and small lattice parameter distortions attributed to tilts or distortions of octahedra and subtle differences in B-site cation ordering, has not been previously reported.

The subtle structural issues in this system make it appropriate to use high-resolution high signal-to-noise SXRD to determine the crystal structure of the undoped parent phase Sr₂FeSbO₆ and the La-doped materials. Rietveld refinements of the host and doped materials were performed using the two monoclinic unit cells (space group $P2_1/n$ and I2/m). All refinements converged smoothly and provided satisfactory agreement parameters. Observed, calculated, and difference plots from the Rietveld refinement of Sr_{1.9}La_{0.1}FeSbO₆ against the SXRD data are shown as an example in Fig. 2A, and the crystal structure together with selected bond lengths for the FeO6 and SbO6 octahedra are depicted in Fig. 2B, while the rest can be found in SI Appendix, Figs. S1–S3. In addition, it is safe to conclude that the oxygen stoichiometry is very close to the nominal value, in part due to the previous neutron diffraction studies and, in addition, for all compositions prepared in this study based on our structural refinements against the collected SXRD data. A close inspection of the low-2θ range, shown in the two inserted plots in Fig. 2A, emphasizes the differences between the two potential monoclinic space groups (space groups $P2_1/n$ and I2/m). It is clearly observed that the Bragg reflections belonging to space group $P2_1/n$ are absent in the SXRD data collected at ambient temperature (marked by arrows in the two insets), which agrees with previously reported (14) ambient temperature NPD data. The absence of primitive Bragg reflections commonly exists in all the refinements of ambient temperature SXRD data collected for the Sr_{2-x}La_xFeSbO₆ (0 $\leq x \leq 0.3$) double-perovskite series. Hence, we assign the body-centered monoclinic unit cell (space group I2/m) to the ambient temperature crystal structure of the undoped parent phase Sr₂FeSbO₆ and the La-doped materials. As is the case for many perovskites, the monoclinic distortion of the cubic perovskite cell is primarily due to the tilting of the octahedra.

There are only two units of charge difference between the two B-site cations Fe³⁺ and Sb⁵⁺ and, although they are quite different chemically, their effective ionic radii are quite close (for high-spin Fe³⁺: r = 0.645 Å; and for Sb⁵⁺: r = 0.60 Å) (26). Thus, it is widely accepted that a certain extent of antisite disorder can exist in this material (9-14). Therefore, we carefully examined the degree of B-site cation ordering in our $Sr_{2-x}La_xFeSbO_6$ (0 $\leq x \leq 0.3$) double-perovskite series by refining the site-fraction occupancy for the two crystallographically independent B-cation sites. The refinement results show that the degree of ordering is about 95% in our undoped parent phase Sr_2FeSbO_6 (x = 0), which is higher than the values reported previously (9-14). This difference can be attributed to the synthetic conditions employed in the current study: Multiple high-temperature (1,500 °C) firings of the ceramic mixture aid the B-site cation ordering, which was also mentioned in a previous neutron diffraction study (14). In contrast, the degree of ordering in our La-doped materials (x = 0.1, 0.2, 0.3) is 100%, i.e., no antisite disorder is observed. Hence, the two crystallographically independent B-cation sites were assigned to Fe3+ and Sb⁵⁺, respectively, just like other fully ordered double perovskites (6, 27). The structural parameters and crystallographic positions of Sr_{1.9}La_{0.1}FeSbO₆ thus determined are presented in Table 1 and those of the remaining compositions can be found in *SI Appendix*, Tables S1–S3.

To further confirm the success of the La³⁺-for-Sr²⁺ substitution in our materials, the lattice parameters for $Sr_{2-x}La_xFeSbO_6$ ($0 \le x \le 0.3$) were extracted from Rietveld refinements of the SXRD data and are plotted against the doping level x in Fig. 3. In general, the lattice parameters a, b, and c and cell volume V all get larger, while the angle β evolves from slightly above 90° to slightly less than 90° (90 + δ formally, not 90 - δ) with La-doping. The changes in these parameters between x = 0 and 0.1 are quite sharp, while

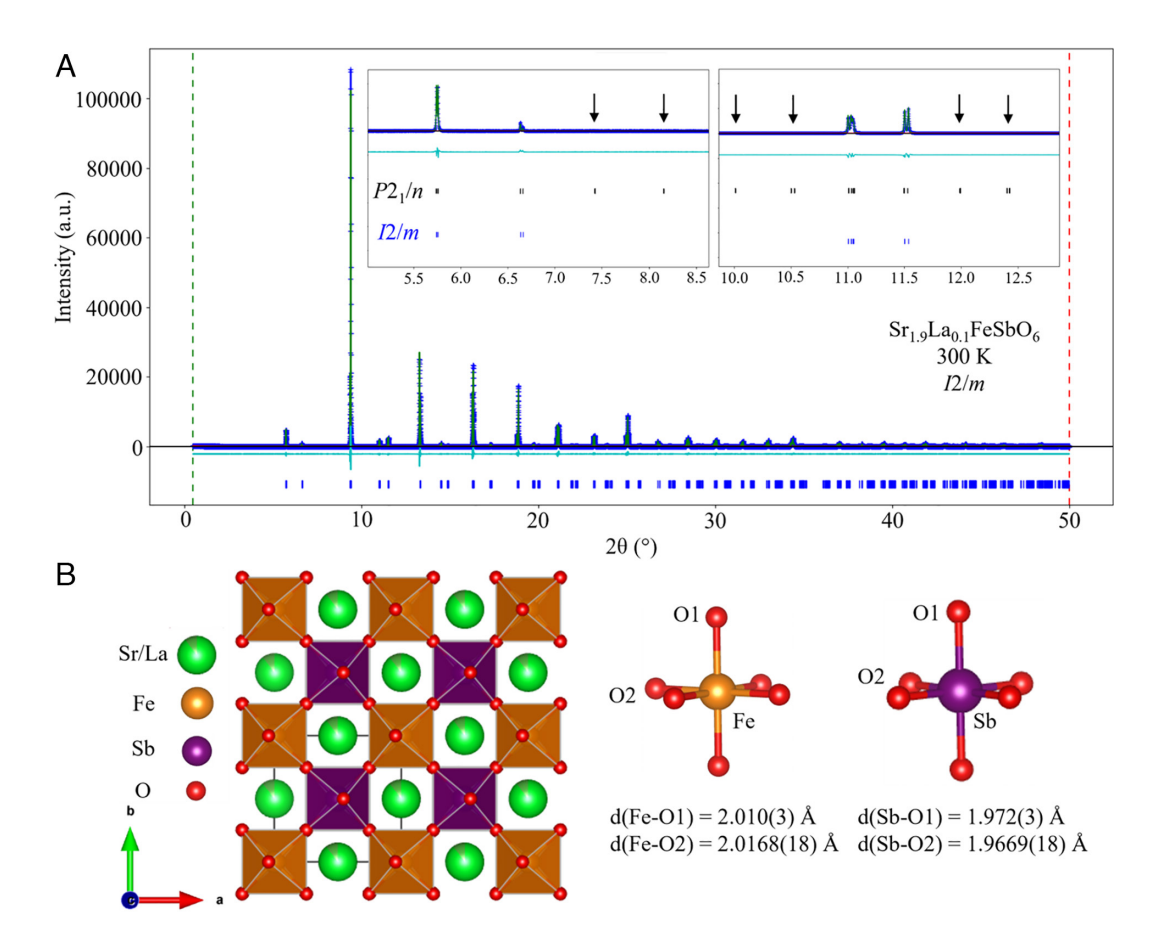


Fig. 2. (A) Observed (blue), calculated (green), and difference (cyan) plots from the Rietveld refinement of $Sr_{1.9}La_{0.1}FeSbO_6$ (space group I2/m) against the SXRD data collected at ambient temperature; insets show in detail the absence of primitive Bragg reflections associated with the $P2_1/n$ symmetry in our data (positions marked by arrows). (B) The structural model for $Sr_{1,9}La_{0,1}FeSbO_6$ together with selected bond lengths for the FeO_6 octahedron and the SbO_6 octahedron.

those between later compositions are much shallower, consistent with the qualitative change from partial ordering to complete ordering among the B-site cations. The effective ionic radius of the La^{3‡} (r = 1.032 Å) (26) dopant is actually smaller than the original A-site cation Sr^{2+} (r = 1.18 Å) (26), and hence, a naive view might be that there should be shrunken lattice parameters.

The unit cell expansion observed can be attributed, however, in an ionic model, to the significantly larger Fe^{2+} (r = 0.78 Å) centers in some of octahedra compared to the original Fe^{3+} (r = 0.645 Å) centers. This formal introduction of Fe^{2+} occurs as a consequence of the La³⁺-for-Sr²⁺ substitution used to raise the Femi Level of this material into the flat bands.

Table 1. Structural parameters and crystallographic positions from the refinement of SXRD data collected from Sr_{1.9}La_{0.1}FeSbO₆ at 300 K

Atoms	x/a	y/b	z/c	S.O.F.	U _{iso} equiv. (Ų)
Sr1	0.49917(16)	0	0.25004(5)	0.95	0.00416
La1	0.49917(16)	0	0.25004(5)	0.05	0.00416
Fe1	0	0	0	1	0.0009
Sb1	0	0	0.5	1	0.0004
O1	-0.0438(5)	0	0.25219(31)	1	0.0039
02	0.25276(31)	0.25307(31)	0.0230(3)	1	0.0097

 $Sr_{1.9}La_{0.1}FeSbO_6$ space group I2/m (#12)

Formula weight: $453.969 \text{ g mol}^{-1}$, Z = 2

 α = 5.62104(1) Å, b = 5.59656(1) Å, c = 7.90033(1) Å, β = 89.9969(6) °, V = 248.5326(8) Å³

Radiation source: Beamline 11-BM at a wavelength of ~0.4590 Å

Temperature: 300 K

wR = 13.791 %; GOF = 1.95

Note: The S.O.F. of the A-site cations (Sr and La) are assigned based on the original stoichiometry ratio of elements put in during the sample preparation.

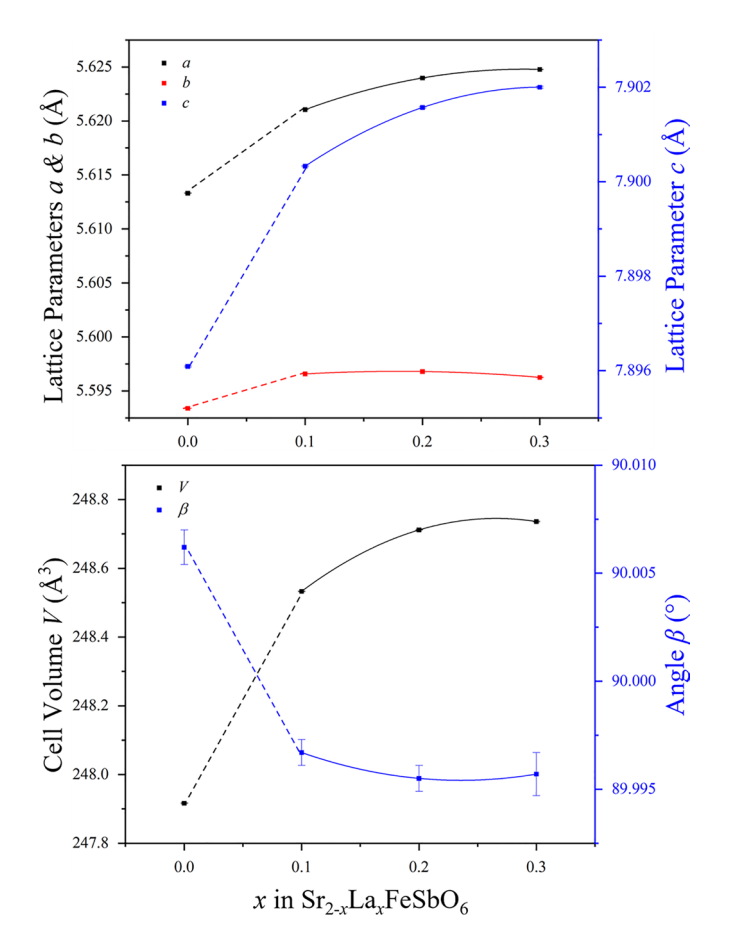


Fig. 3. Refined lattice parameters a, b, and c, cell volume V, and angle β plotted for each composition of the $Sr_{2x}La_xFeSbO_6$ series.

Origin of the Flat Bands. The Sr_2FeSbO_6 double perovskite crystallizes in space group I2/m; the spin structure for the calculations was set to antiferromagnetic based on our experimental data and the literature (12, 14). The calculated band structure and electronic density of states (DOS) of the undoped parent phase Sr_2FeSbO_6 are depicted in Fig. 4A. The states close to the Fermi level arise from Fe-d, and O-p states while the Sb-s states lie higher in energy. Due to the octahedral environment, the Fe-d orbitals are split into t_{2g} and e_g groups, with the t_{2g} group giving rise to the flat bands as shown in Fig. 4B. Spin-orbit coupling (SOC) has a negligible effect on the bands near the Fermi energy and neither does the choice of Hubbard U as long as it is larger than a minimal value, in agreement with other similar Fe oxides (28).

The tight-binding (TB) model of the Fe- t_{2g} states was constructed using Wannier90 functions (29) to investigate the origin of the flat bands. It was found that the Wannier Hamiltonian from the Fe- t_{2g} states consist of contributions from both direct Fe-Fe electron hopping and indirect (assisted by Fe-O and Sb-O orbital overlap) electron hopping. Fig. 4C shows a comparison between the actual t_{2g} spectrum (which includes both direct and indirect electron hopping) and a spectrum that considers only direct hopping. It is found that the d_{xx} and d_{yx} states are slightly affected by indirect hopping and that the d_{xy} - d_{xy} hopping probability (i.e., the sub-band energy width) is increased by five times. Hence, the direct Fe-Fe electron hopping probability, which is small, is enhanced by the indirect electron hopping coming from Fe-O and Sb-O states for the Fe d_{xy} orbitals, and to a much lesser but significant degree for the d_{xx} orbitals. Due to the only weakly broken fourfold rotational symmetry parallel to c, the contribution

of indirect electron hopping to the total electron hopping probability in the xy plane is largest. That is, the presence of a fourfold rotational symmetry parallel to c implies zero out-of-plane electron hopping. In fact, it is much larger than the direct hopping, as is evidenced in Fig. 4C. Furthermore, among the d_{yz} and d_{xz} orbitals, one of the sub-bands (d_{yz}) is significantly flatter than the other. The origin of this very flat sub-band can be attributed to the interference of electron hopping instead of its absence. Namely, the in-plane d_{xz} , d_{yz} hoppings are close (in parameter space) to a Hamiltonian with a completely flat band in the $k_x - k_y$ plane. All the details for the theoretical calculations are provided in the SI Appendix.

Physical Property Characterization.

Magnetic properties. The zero-field-cooled (ZFC) and fieldcooled (FC) temperature-dependent DC magnetization data were collected for each composition of the Sr_{2-x}La_xFeSbO₆ $(0 \le x \le 0.3)$ double-perovskite series under an applied field of H = 0.1 T and then plotted as magnetic susceptibility χ against temperature (Fig. 5A). A divergence between the ZFC and FC curves is clearly observed for each composition after going through a local maximum in the magnetic susceptibility. This behavior marks the onset of magnetic ordering. Thus, the DC magnetic susceptibility data, over the suitable temperature range (selected as the straight-line part of the $1/\chi$ vs. T curves, marked in red in Fig. 5B) for each composition were fitted to the Curie–Weiss law $[\chi = C/(T - \theta) + \chi_0]$, to yield the Curie constants C, Weiss temperatures $\theta,$ and effective moments μ_{eff} that are listed in Table 2. The field-dependent magnetization data were collected from each composition as well, at T = 300 K and 1.8 K, and are plotted as M against H (-9 \leq H / T \leq 9) in Fig. 5 C and D, respectively.

The undoped parent phase Sr_2FeSbO_6 (x = 0) has been reported to adopt long-range, A-type (i.e., type I) antiferromagnetic ordering based on low-temperature neutron powder diffraction (NPD) data (12). The ZFC temperature-dependent magnetization data collected from our Sr₂FeSbO₆ shows an antiferromagnetic transition around $T_N \approx 33$ K, in good agreement with the literature. However, a second transition ($T_A \approx 15 \text{ K}$) is observed in every batch of this compound at lower temperature. Based on the structural refinement against the high-intensity high-resolution synchrotron XRD data, the presence of a minority phase in the parent compound is unlikely, and hence we believe that the transition at T_A is intrinsic. This observation suggests that an additional feature apart from the well-established antiferromagnetic transition, for example, potentially some glassiness or frustration, is likely to present to a certain extent in the parent compound (Fig. 5 A and B). However, one of the diagnostic features of a typical spin-glass system (low-temperature field-dependent magnetization data displaced from the origin) (30) is absent in our M vs. H plots (Fig. 5 C and D), which could be due to the nearly-fully-ordered character of our sample and the relatively low sensitivity of our M vs. H measurements. To further investigate these two transitions (T_N and T_A), AC magnetic susceptibility data χ' were collected at various frequencies with a small DC field (10 Oe) applied. These data are plotted against temperature T in the inset in Fig. 5A. The transitions are both visible: The one around $T_N \approx 33$ K is relatively resistant to the change in AC frequency, while the transition around $T_A \approx 15$ K is quite labile. This supports the conclusion that the transition at $T_N \approx 33$ K is attributed to long-range antiferromagnetic ordering, while the transition at $T_A \approx 15$ K should be attributed to a less well-defined transition in the system, possibly as a consequence of the small amount of antisite disorder existing between B-cations in the parent compound. The

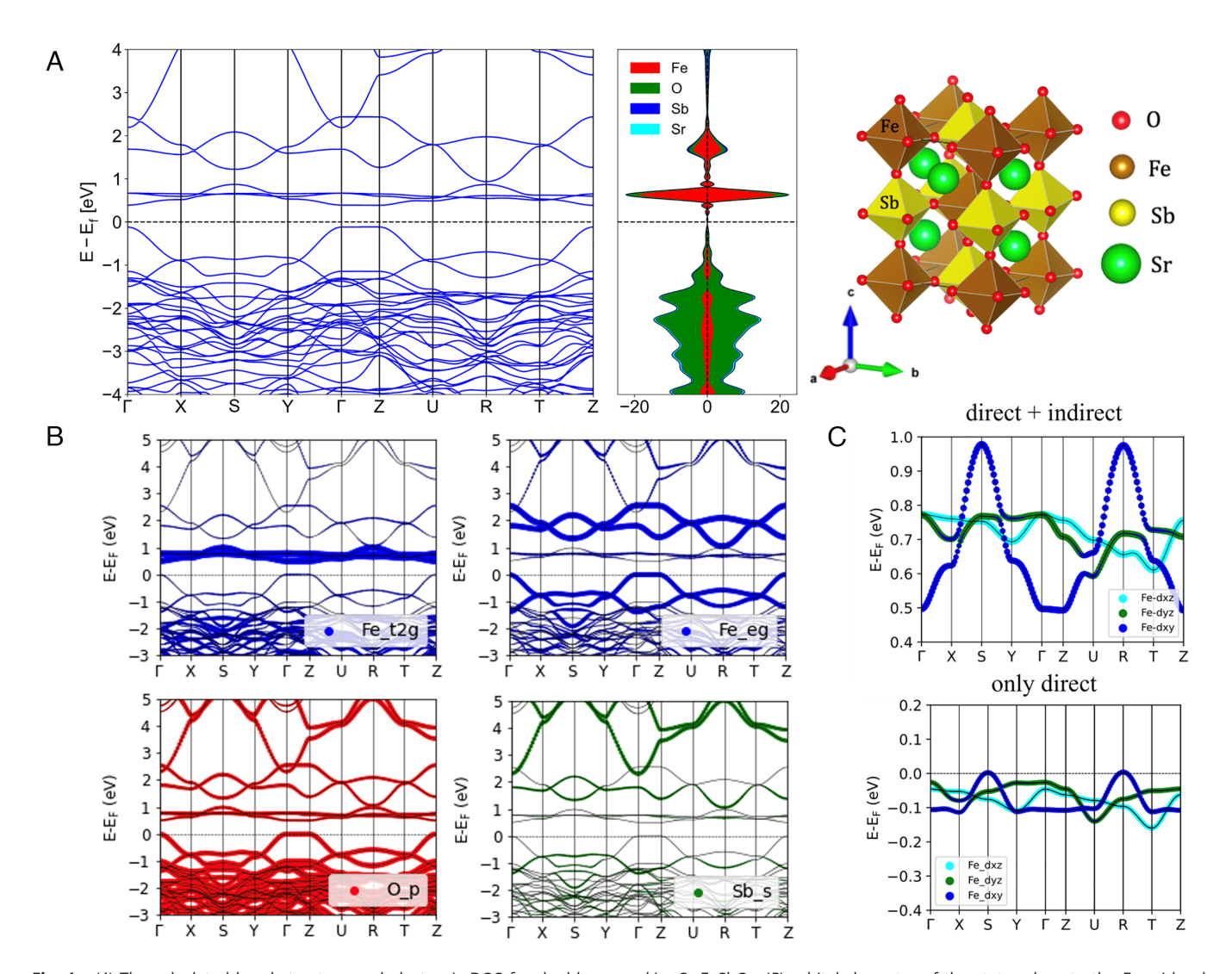


Fig. 4. (A) The calculated band structure and electronic DOS for double-perovskite Sr₂FeSbO₆; (B) orbital character of the states close to the Fermi level; (C) band structure of the Fe- t_{2g} states considering direct + indirect electron hopping and only direct electron hopping.

coexistence of a magnetically ordered spin system and a spin-glass system for the parent compound has been postulated in a previous study (12). Thus, in our case, if the lower temperature transition is assumed to be a spin-glass transition, then that is consistent with expectations that the glassiness vanishes upon La-doping as a result of complete ordering between B-site cations.

The La-doped materials $Sr_{2-x}La_xFeSbO_6$ (x = 0.1, 0.2, 0.3) show a systematic increase in the magnitude of DC magnetic susceptibility, accompanied by a subtle but continuous shift of the local maximum to a lower temperature (Fig. 5 A and B). At 300 K, the isothermal magnetization as a function of applied field for the materials studied is linear and passes through the origin with a

Table 2. The Curie constant and Weiss temperature extracted from the fitting of paramagnetic susceptibility to the Curie-Weiss law, the observed effective moment per formula unit, and the calculated effective moment per formula unit predicted based on the spin-only formula for each composition of the Sr_{2-x}La_xFeSbO₆ series

Composition	Curie constant <i>C</i> (cm³ K mol ⁻¹)	Observed effective moment per formula unit μ _{eff.obs} (μ _B /f.u.)	Calculated effective moment per formula unit $\mu_{eff.cal}$ ($\mu_{B}/f.u.$) (h.s. d ⁵ Fe ³⁺ and l.s. d ⁶ Fe ²⁺)	Calculated effective moment per formula unit $\mu_{eff.cal}$ ($\mu_{B}/f.u.$) (h.s. d ⁵ Fe ³⁺ and i.s. d ⁶ Fe ²⁺)	Calculated effective moment per formula unit $\mu_{eff.cal}$ ($\mu_{B}/f.u.$) (h.s. d ⁵ Fe ³⁺ and h.s. d ⁶ Fe ²⁺)	Weiss temperature θ (K)
Sr _{2-x} La _x FeSbO ₆						
<i>x</i> = 0	3.796(7)	5.511	5.916	5.916	5.916	-169.2(6)
<i>x</i> = 0.1	3.510(7)	5.299	5.324	5.607	5.814	-126.0(6)
<i>x</i> = 0.2	3.019(6)	4.914	4.733	5.299	5.713	-54.6(5)
<i>x</i> = 0.3	2.839(5)	4.766	4.141	4.990	5.611	+5.0(5)

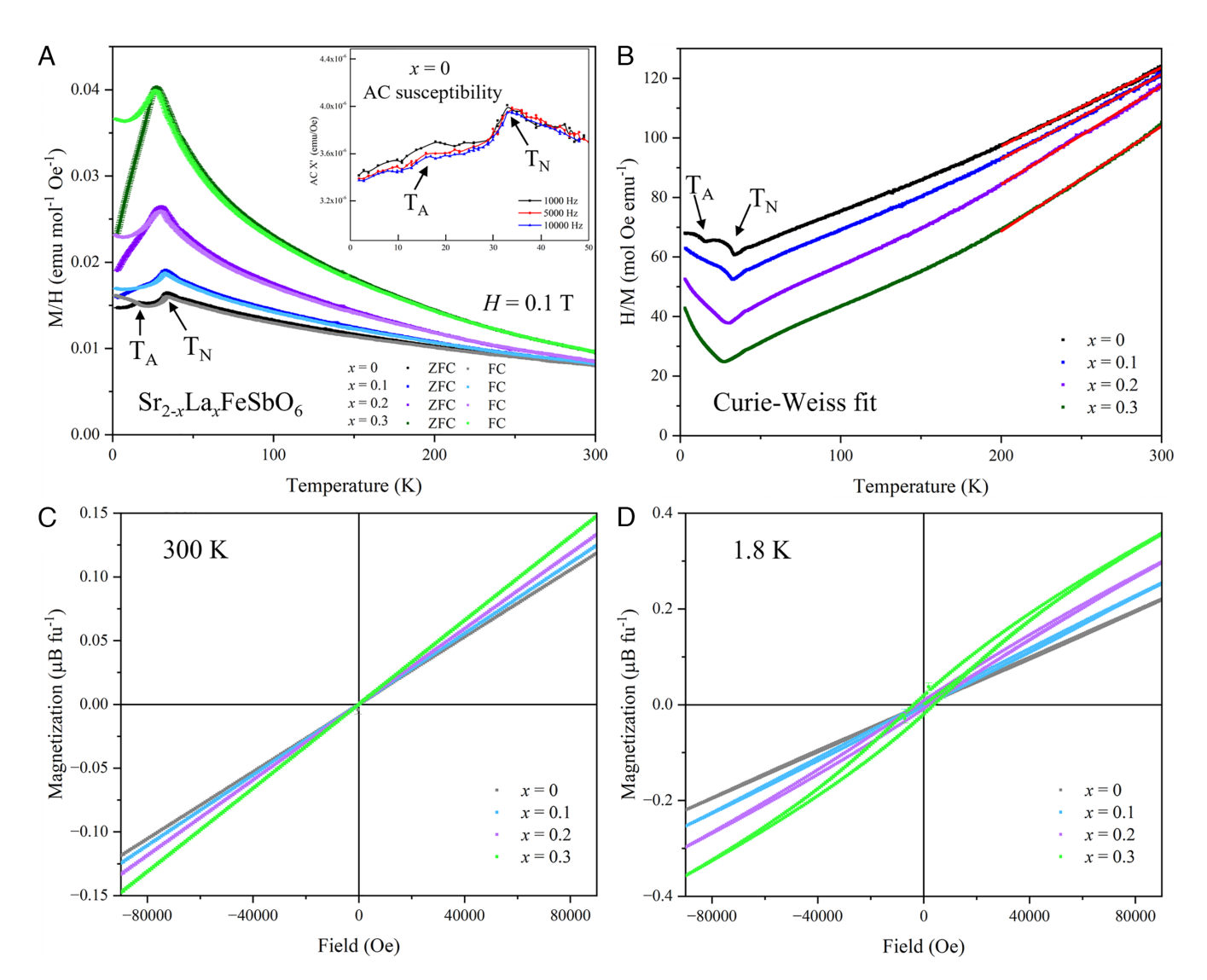


Fig. 5. (*A*) The ZFC and FC temperature-dependent DC magnetization data collected under an applied field of H = 0.1 T; Inset shows the AC magnetic susceptibility data χ' collected from Sr₂FeSbO₆ at various frequencies with a small DC field (10 Oe) applied; (*B*) The inverse of magnetic susceptibility 1/ χ plotted against temperature T, with the straight-line part (marked in red) fitted to the Curie–Weiss law; the field-dependent magnetization data collected at (*C*) 300 K and (*D*) 1.8 K for each composition of the Sr_{2- χ}La_{χ}FeSbO₆ (0 ≤ χ ≤ 0.3) double-perovskite series.

positive slope, while the analogous data collected at 1.8 K exhibit hysteresis with the "loop" systematically opening up upon increasing electron doping (Fig. 5 *C* and *D*), all consistent with temperature-dependent magnetization data.

The Curie constant C (Fig. 6A), Weiss temperature θ (Fig. 6B), and effective moment per formula unit, μ_{eff} (Fig. 6C), extracted from the Curie-Weiss fits of DC magnetic susceptibility data over the same high-temperature range (200 to 300 K), all progress linearly with respect to the La-doping level x. The Curie constant C extracted from Sr_2FeSbO_6 (x = 0) is 3.796(7) cm³ K mol⁻¹ and hence yields an observed μ_{eff} value of 5.511 $\mu_{B}/\text{f.u.},$ corresponding to ~93% of the expected spin-only value for an S = 5/2 system (Fig. 6A). Since Fe³⁺ in this case undoubtedly exhibits a high-spin (h.s.) d⁵ configuration, and upon formal reduction to Fe²⁺ due to the La³⁺-for-Sr²⁺ substitution, the number of unpaired electrons should decrease independent of whether the Fe²⁺ displays highspin (h.s.), intermediate-spin (i.s.), or low-spin (l.s.) d⁶ configuration (Fig. 6D). If the overall observed effective moment $\mu_{\rm eff}$ is a linear combination of Fe³⁺ and Fe²⁺ centers in our materials, an expected effective moment μ_{eff} can be calculated from the spinonly formula. The observed effective moment μ_{eff} (black solid line)

is plotted together with the calculated ones (normalized to the value at 0 electron doping) for all three scenarios (red dotted line for h.s.+ l.s., green dotted line for h.s.+ i.s., and blue dotted line for h.s.+ h.s.) in Fig. 6C. Our experimental data thus suggest a possibility of high-spin d^5 Fe³⁺ plus intermediate-spin d^6 Fe²⁺ scenario for our materials, even though O²⁻ is a relatively weak field ligand, which in principle should favor the high-spin electronic configuration of a 3d transition metal like Fe. The intermediate-spin configuration of Fe^{2+} (S = 1) is not commonly seen, but a few intermediate-spin iron(II) complexes have been reported in the literature (31–33). Another possible explanation for what may appear to be an unusual intermediate-spin Fe²⁺ ion is, contrary to the case where all the spin values deduced are based on a localized spin picture, that in this flat-band electronic system, in which the doped electrons are in a complex band, the effective moment per doped electron is actually lower than expected from a combination of localized high-spin d⁵ Fe³⁺ plus localized high-spin d⁶ Fe²⁺. We also note that for all the materials studied here, the temperature dependence of the magnetic susceptibility deviates from strict Curie Weiss behavior on decreasing the temperature below about 150 K. We have no data that indicate why this is the case.

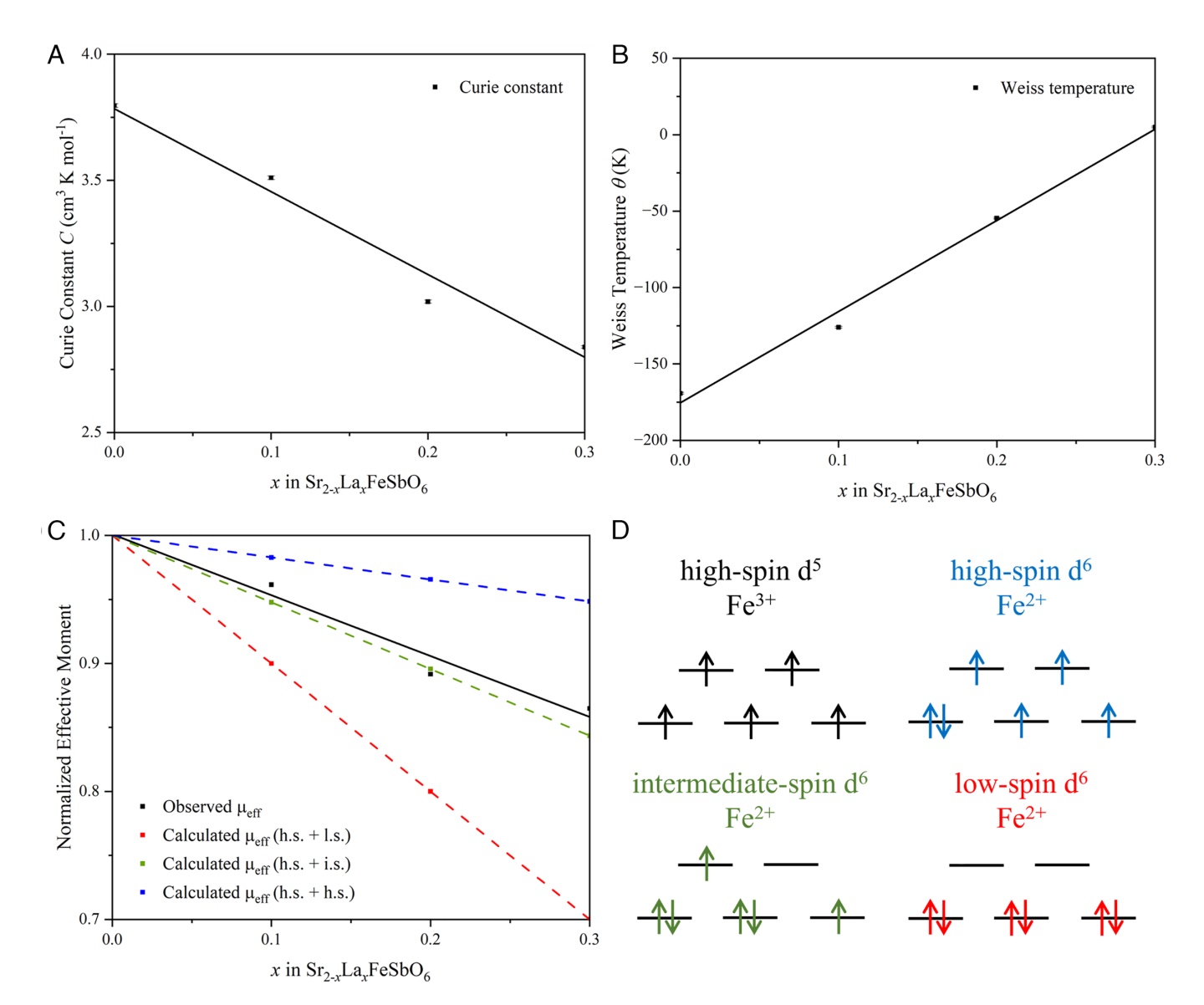


Fig. 6. (A) The Curie constant and (B) the Weiss temperature extracted from the fitting of paramagnetic susceptibility to the Curie-Weiss law; (C) The normalized observed effective moment per formula unit plotted against the normalized effective moment per formula unit calculated from the spin-only contribution based on three possible combinations of spin configurations for each composition of the $Sr_{2x}La_xFeSbO_6$ ($0 \le x \le 0.3$) double-perovskite series; (D) Possible spin configurations of Fe³⁺ and Fe²⁺ centers.

The Weiss temperature θ progresses from a large negative value to a small positive value with increasing La-dopant concentration (Fig. 6B). This indicates that the antiferromagnetic coupling between ferromagnetically ordered moments that dominates the bulk magnetic behavior of Sr₂FeSbO₆ (an A-type antiferromagnet) is significantly weakened by introducing the electrons. At the threshold composition of the single-phase solid solution studied here (x = 0.3), the ferromagnetic coupling within the layers eventually outweighs the competing antiferromagnetic interactions between layers. Magnetic characterization at higher temperatures, which is not available in our laboratory, may be of interest in future studies designed to investigate the magnetism of these materials above room temperature.

Heat capacity. Heat capacity data were collected from both end members of the $Sr_{2-x}La_xFeSbO_6$ (0 $\leq x \leq 0.3$) double-perovskite series: the undoped parent phase (x = 0) at various external applied fields ($\mu_0 H = 0, 3, 6, 9 \text{ T}$) and the threshold composition (x = 0.3) at zero applied field. Data were also collected for the nonmagnetic analog Sr₂GaSbO₆ at zero applied field over the temperature range $1.8 \le T / K \le 50.$

The total heat capacity C_{total} data are plotted against temperature in Fig. 7A. The peak observed in C_{total} curves of the undoped parent phase Sr_2FeSbO_6 near $T \approx 33$ K is again seen to be relatively resistant to changes in the external applied field, corresponding to the phase transition associated with bulk long-range antiferromagnetic ordering observed in the temperature-dependent magnetization data. The lower temperature transition (T \approx 15 K) observed in the magnetic susceptibility cannot clearly be seen in the total heat capacity Ctotal curve, consistent with the possibility that only a small amount of glassiness is present in the system due to the limited antisite disorder. Furthermore, the feature around $T \approx 33$ K which is associated with the long-range antiferromagnetic ordering in the undoped parent phase Sr₂FeSbO₆ is absent in analogous total heat capacity data C_{total} collected from the threshold composition $Sr_{1.7}La_{0.3}FeSbO_6$, x=0.3. This is unusual and suggests that the phase transition due to long-range antiferromagnetic ordering has been significantly suppressed in the doped sample in spite of its significant drop in susceptibility near 30 K. The introduction of the La³⁺ dopant seems to severely interfere with the original long-range A-type antiferromagnetic

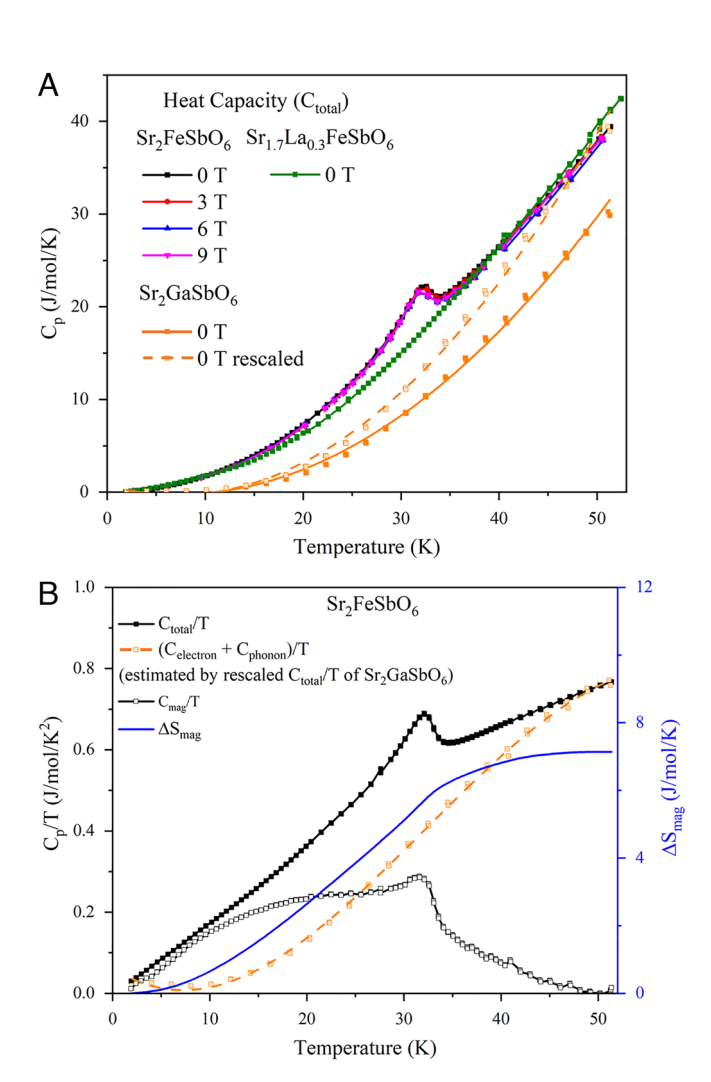


Fig. 7. (A) The total heat capacity C_{total} plotted against temperature for Sr_2FeSbO_6 at H=0,3,6,9 T field applied, $Sr_{1.7}La_{0.3}FeSbO_6$, and Sr_2GaSbO_6 at zero field applied; (B) All relevant Cp/T plotted against temperature T to extract the magnetic contribution to heat capacity and entropy change in Sr₂FeSbO₆.

ordering in the undoped material, hence yielding the disappearance of a signature λ -shaped transition in the thermodynamic data collected from the threshold composition. This peculiar feature postulates that the transition observed in the magnetic susceptibility of Sr_{1.7}La_{0.3}FeSbO₆ may not be long-range and its origin may be of future interest.

The total heat capacity of a magnetic material can be interpreted as the sum of electronic, phonon, and magnetic contributions $(C_{total} = C_{electron} + C_{phonon} + C_{mag})$. Thus, to isolate the magnetic contribution C_{mag} to determine the magnetic entropy change ΔS_{mag} , the heat capacity contributions due to electrons ($C_{electron}$) and phonons (C_{phonon}) need to be estimated and subtracted. To make this approximation, the heat capacity data collected from Sr₂GaSbO₆, a nonmagnetic analog of Sr₂FeSbO₆, has been rescaled here to minimize the nonmagnetic differences between Fe3+ and Ga3+, hence serving as an approximation for Cphonon of Sr_2FeSbO_6 . $C_{electron}$ is effectively = 0 for insulating materials such as these (the resistivity of all the materials prepared in this study is too high to measure at ambient temperature and increases with decreasing temperature meaning that there are no conduction electrons present that would yield a significant C_{electron}). The resulting C_D/T is plotted against temperature in Fig. 7B. After subtracting the approximate phonon contributions, equivalent to rescaled Ctotal/T of Sr₂GaSbO₆, an approximate magnetic contribution

C_{mae}/T of Sr₂FeSbO₆ can be extracted. Then, the magnetic entropy change ΔS_{mag} can be estimated to yield a saturation value of -7.14J/mol/K, which corresponds to - 48% of that expected for Heisenberg spin (for an S = 5/2 system (Fe³⁺: high-spin d⁵)) ordering, $R \ln (2S + 1) = 14.89 \text{ J/mol/K}$. The experimental value is much closer to the Ising spin prediction $R \ln (2) = 5.76 \text{ J/mol/K}$. We therefore tentatively conclude that the magnetic entropy released at the magnetic phase transition is associated with the bulk long-range ordering of spins in Sr₂FeSbO₆ that are closer to Ising-like than Heisenberg-like.

Basic optical properties. The diffuse reflectance spectra were collected from powder samples at ambient temperature in order to observe the evolution of the optical absorption behavior in the $Sr_{2-x}La_xFeSbO_6$ (0 $\leq x \leq 0.3$) double-perovskite series. The pseudoabsorbance, transferred from the reflectance using the Kubelka-Munk function, is plotted against wavelength (nm) in Fig. 8. The optical transitions were then analyzed based on Tauc plots via the direct-transition approach, as shown in the *Inset.* The energy scales determined for these direct transitions, which for the La-doped material do show a gradual decreasing trend (from 2.58 eV to 2.24 eV) with increasing La-dopant concentration. Thus, the La-for-Sr substitution has a relatively small effect on the band gap, which is below the Fermi energy for the doped compositions, but the electrons in the narrow band do not yield a strong optical effect. Experimental work exploring more extreme conditions or different electron dopants to overcome the current solubility threshold in this system may be of future interest.

Conclusions

Based on theoretical insights into the flat electronic bands expected to lie above the Fermi Energy in this double-perovskite system, the parent phase Sr₂FeSbO₆ and its La³⁺-for-Sr²⁺-substituted phases were prepared via traditional high-temperature ceramic synthesis. Their structural and physical properties were characterized. $Sr_{2-x}La_xFeSbO_6$ (0 $\leq x \leq 0.3$) double perovskites crystallize in a monoclinic symmetry space group (I2/m) based on high-resolution SXRD data collected at ambient temperature. A small amount of antisite disorder exists in our Sr₂FeSbO₆ (~95% degree of B-cation ordering) and vanishes when the

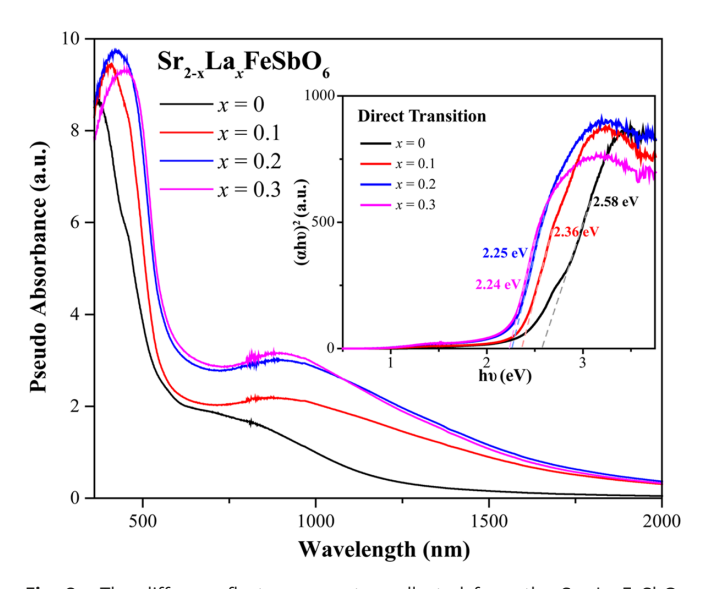


Fig. 8. The diffuse reflectance spectra collected from the Sr_{2-x}La_xFeSbO₆ $(0 \le x \le 0.3)$ double-perovskite series with the energy scales of optical transitions extracted from Tauc plots obtained by using a direct transition equation.

La-dopant is introduced into the system. These subtle structural changes are reflected in the physical properties of these materials. Sr₂FeSbO₆ possesses two intrinsic transitions in magnetic susceptibility data. The first one at $T_N \approx 33$ K is attributed to the bulk long-range antiferromagnetic ordering. The origin of the second transition at $T_A \approx 15$ K is unclear but may be due to the small amount of spin-freezing/frustration in the system which disappears upon La-doping as a result of complete ordering between B-site cations in doped materials. The magnetization data collected from doped materials also suggest that the antiferromagnetic coupling used to dominate the bulk magnetic behavior is weakened by introducing the La³⁺ dopant into the system, and the dominant coupling between spins eventually becomes weakly ferromagnetic at the threshold composition Sr_{1.7}La_{0.3}FeSbO₆. The parameters extracted from the Curie–Weiss fit and the calculated band structures support the idea that in a localized moment picture some of the d⁵ Fe³⁺ centers are reduced to d⁶ Fe²⁺ centers upon La³⁺-for-Sr²⁺ substitution. Heat capacity data collected from two end members of our double-perovskite series, Sr₂FeSbO₆ and Sr_{1.7}La_{0.3}FeSbO₆, completely agree with the collected magnetization data. In addition to the magnetic properties, the optical transitions experimentally evaluated were found to gradually decrease in energy scale with increasing La-dopant concentration, suggesting that the material does not fit into in a strictly "rigid band" scenario. The theoretical picture and experimental data thus suggest that the electron-doped double-perovskite Sr₂FeSbO₆ may be an unusual electronic system worthy of further study due to the potential electron occupancy of its flat electronic band. Furthermore, Sr₂FeSbO₆ is certainly not the sole example in this material family that is with flat electronic bands near or at the fermi level, other candidates such as the Cr-analog are of future interest as well.

Materials and Methods

Materials Synthesis. Approximately 1.0 g polycrystalline powder samples of the $Sr_{2-x}La_x$ FeSbO₆ ($0 \le x \le 0.5$) double perovskites were prepared via traditional high-temperature ceramic synthesis. Stoichiometric amounts of SrCO₃ (Alfa Aesar, 99.99%), La₂O₃ (Alfa Aesar, 99.99%, dried at 900 °C), Fe₃O₄ (Alfa Aesar, 99.997%), and Sb₂O₅ (Alfa Aesar, 99.998%) were thoroughly ground together by using an agate mortar and pestle and then transferred into an alumina crucible for calcinations in air. These reaction mixtures were first slowly (1 °C/min) ramped up to 1,000 °C and held overnight to decompose the carbonate, and then were annealed at 1,500 °C (temperature raised at 3 °C/min) for two periods of 48 h with intermittent grindings. A powder sample of Sr₂GaSbO₆, as the nonmagnetic analog of undoped parent phase Sr₂FeSbO₆, was prepared as previously described (34) to provide a nonmagnetic phonon standard for the heat capacity measurements.

X-ray Powder Diffraction Measurements and Refinements. The reaction progress was monitored using laboratory X-ray powder diffraction data collected

- P. Schiffer, A. P. Ramirez, W. Bao, S.-W. Cheong, Low temperature magnetoresistance and the magnetic phase diagram of La_{1.x}Ca_xMnO₃. Phys. Rev. Lett. **75**, 3336–3339 (1995).
- J. G. Bednorz, K. A. Müller, Possible highT c superconductivity in the Ba-La-Cu-O system. Zeitschrift für Physik B Condensed Matter 64, 189-193 (1986).
- R. E. Cohen, Origin of ferroelectricity in perovskite oxides. Nature 358, 136-138 (1992).
- P. Lacorre, F. Goutenoire, O. Bohnke, R. Retoux, Y. Lallgant, Designing fast oxide-ion conductors based on La2Mo2O9. Nature 404, 856-858 (2000).
- R. Asahi, T. Morikawa, T. Ohwaki, K. Aoki, Y. Taga, Visible-light photocatalysis in nitrogen-doped titanium oxides. Science 293, 269-271 (2001).
- S. Vasala, M. Karppinen, A₂B'B"O₆ perovskites: A review. Prog. Solid State Chem. 43, 1-36 (2015).
- M. T. Anderson, K. B. Greenwood, G. A. Taylor, K. R. Poeppelmeier, B-cation arrangements in double perovskites. *Prog. Solid State Chem.* **22**, 197–233 (1993).
- G. King, P. M. Woodward, Cation ordering in perovskites. J. Mater Chem. 20, 5785-5796 (2010).
- G. Blasse, New compounds with perovskite-like structures. J. Inorg. Nucl. Chem. 27, 993-1003 (1965)

at room temperature on a Bruker D8 FOCUS diffractometer (Cu K α) over a 2 θ range between 5° and 70°. Once the reactions were deemed finished, laboratory XRD data with much better statistical significance, covering a 20 range between 5° and 110°, were collected from each sample to establish the sample purity. The high-resolution SXRD data were acquired at Beamline 11-BM at the Advanced Photon Source at Argonne National Laboratory at a wavelength of ~ 0.4590 Å. Detailed structural refinements were performed by the Rietveld method (35) using the GSAS-II program, with crystal structures visualized by the VESTA program.

Magnetization and Thermodynamic Measurements. The magnetization data were collected using the ACMS II and VSM options of a Quantum Design Physical Property Measurement System (PPMS). Temperature-dependent magnetization (M) data were collected under an applied external field (H) of 1,000 Oe. Magnetic susceptibility is defined as M/H. Field-dependent isothermal magnetization data between H = 90,000 Oe and -90,000 Oe were collected at T = 300 K and 1.8 K. Heat capacity was measured using a standard relaxation method in the PPMS over the temperature range 1.8 to 50 K.

Optics Measurements. The diffuse reflectance spectra were collected from a powder sample of each composition at ambient temperature on a Cary 5000i UV-VIS-NIR spectrometer equipped with an internal DRA-2500 integrating sphere. The data were converted from reflectance to pseudo absorbance via applying the Kubelka-Munk function, and band gaps were calculated from Tauc plots by using a direct transition equation (36).

Theoretical Calculations. Density-functional-theory-based (DFT) first-principles calculations were performed using the projector augmented-wave (PAW) method as implemented in the VASP code (37, 38). The generalized gradient approximation (GGA) was employed to deal with electron correlation (39). Reciprocal space integrations were completed over a $7 \times 7 \times 5$ Monkhorst-Pack k-point mesh. The energy cutoff was chosen to be 1.5 times as large as the values recommended for the relevant PAW pseudopotentials. SOC had an insignificant effect on the bands, and we therefore ignored it in our analysis. The Hubbard U was set to 3 eV, as in other similar iron oxides (28). To study the flat-band properties of the compound, we obtained a real space tight-binding Hamiltonian using the maximally localized Wannier functions (MLWFs) approach (29).

Data, Materials, and Software Availability. All study data are included in the article and/or SI Appendix.

ACKNOWLEDGMENTS. The experimental research was primarily done at Princeton University, supported by the US Department of Energy Division of Basic Energy Sciences, through the Institute for Quantum Matter, Grant No. DE-SC0019331. The theory work was supported by the European Research Council (ERC) under the European Union's Horizon 2020 research and innovation programme (grant agreement No. 101020833), the ONR Grant No. N00014-20-1-2303, Simons Investigator Grant No. 404513, the Gordon and Betty Moore Foundation through the EPiQS Initiative, Grant GBMF11070 and Grant No. GBMF8685, NSF-MRSEC Grant No. DMR-2011750, BSF Israel US foundation Grant No. 2018226, and the Princeton Global Network Funds. Use of the Advanced Photon Source at Argonne National Laboratory was supported by the US Department of Energy, Office of Science, Office of Basic Energy Sciences, under Contract No. DE-AC02-06CH11357.

- 10. P. D. Battle, T. C. Gibb, A. J. Herod, J. P. Hodges, Sol-gel synthesis of the magnetically frustrated oxides Sr₂FeSbO₆ and SrLaFeSnO₆. J. Mater. Chem. 5, 75–78 (1995).
- S.-O. Lee, T. Y. Cho, S.-H. Byeon, Magnetic property of the perovskite Fe(III) oxide. Bull. Korean Chem. Soc. 18, 91-97 (1997).
- 12. E. J. Cussen, J. F. Vente, P. D. Battle, T. C. Gibbb, Neutron diffraction study of the influence of structural disorder on the magnetic properties of Sr₂FeMO₆ (M=Ta, Sb). J. Mater. Chem. 7, 459-463
- 13. N. Kashima, K. Inoue, T. Wada, Y. Yamaguchi, Low temperature neutron diffraction studies of Sr₂FeMO₆ (M=Nb, Sb). Appl. Phys. A 74, 805-807 (2002).
- 14. A. Faik, J. M. Igartua, E. Iturbe-Zabalo, G. J. Cuello, A study of the crystal structures and the phase transitions of Sr₂FeSbO₆, SrCaFeSbO₆ and Ca₂FeSbO₆ double perovskite oxides. J. Mol. Struct. 963, 145-152 (2010).
- L. Jin et al., Magnetic cations doped into a double perovskite semiconductor. J. Mater. Chem. C Mater. 10, 3232-3240 (2022).
- N. Regnault et al., Catalogue of flat-band stoichiometric materials. Nature 603, 824-828 (2022).

- 17. F. Xie, Z. Song, B. Lian, B. A. Bernevig, Topology-bounded superfluid weight in twisted bilayer graphene. Phys. Rev. Lett. 124, 167002 (2020).
- V. Peri, Z. Song, B. A. Bernevig, S. D. Huber, Fragile topology and flat-band superconductivity in the strong-coupling regime. Phys. Rev. Lett. 126, 027002 (2021).
- C. Z. Chang et al., Experimental observation of the quantum anomalous Hall effect in a magnetic topological Insulator. Science 340, 167-170 (2013).
- C. Z. Chang et al., High-precision realization of robust quantum anomalous Hall state in a hard ferromagnetic topological insulator. *Nat. Mater.* **14**, 473–477 (2015).

 M. Serlin *et al.*, Intrinsic quantized anomalous Hall effect in a moiré heterostructure. *Science* **367**,
- 900-903 (2020).
- D. Călugăru et al., General construction and topological classification of crystalline flat bands. Nat. Phys. 18, 185-189 (2022).
- Y. Cao et al., Correlated insulator behaviour at half-filling in magic-angle graphene superlattices. Nature 556, 80-84 (2018).
- R. Bistritzer, A. H. MacDonald, Moiré bands in twisted double-layer graphene. Proc. Natl Acad. Sci. U.S.A. 108, 12233-12237 (2011).
- Y. Cao et al., Unconventional superconductivity in magic-angle graphene superlattices. Nature 556, 43-50 (2018).
- R. D. Shannon, Revised effective ionic radii and systematic studies of interatomic distances in halides and chalcogenides. Acta Crystallogr. A 32, 751-767 (1976).
- L. Jin et al., Structure and properties of the $Sr_2In_{1\star}Sn_{\star}SbO_6$ double perovskite. J. Solid State Chem. 314, 123355 (2022).
- H. Hsu, K. Umemoto, M. Cococcioni, R. M. Wentzcovitch, The hubbard U correction for iron-bearing minerals: A discussion based on (Mg, Fe)Si₀3 perovskite. Phys. Earth Planet. Inter. 185, 13-19 (2011).

- 29. A. A. Mostofi et al., An updated version of wannier90: A tool for obtaining maximally-localised Wannier functions. Comput. Phys. Commun. 185, 2309-2310 (2014).
- J. E. Page, M. A. Hayward, $CaMn_{0.5}Ir_{0.5}O_{2.5}$: An anion-deficient perovskite oxide containing Ir^{3+} Inorg. Chem. 58, 8835-8840 (2019).
- M.-S. Liao, J. D. Watts, M.-J. Huang, Electronic structure of some substituted iron(II) porphyrins. Are they intermediate or high spin? J. Phys. Chem. A 111, 5927-5935 (2007).
- 32. J. F. Kirner, W. Dow, W. Robert, Scheidt, Molecular stereochemistry of two intermediate-spin complexes. Iron(II) phthalocyanine and manganese(II) phthalocyanine. Inorg. Chem. 15, 1685-1690 (2002).
- J. C. Ott, H. Wadepohl, M. Enders, L. H. Gade, Taking solution proton NMR to its extreme: Prediction and detection of a hydride resonance in an intermediate-spin iron complex. J. Am. Chem. Soc. 140, 17413-17417 (2018).
- L. Jin et al., Ferromagnetic double perovskite semiconductors with tunable properties. Adv. Sci. 9, 2104319 (2022).
- H. Rietveld, A profile refinement method for nuclear and magnetic structures. J. Appl. Crystallogr. 2, 65-71 (1969).
- A. Y. Tarasova et al., Electronic structure and fundamental absorption edges of KPb₂Br5, $k_{0.5}Rb_{0.5}Pb_2Br_5$, and $RbPb_2Br_5$ single crystals. J. Phys. Chem. Solids **73**, 674–682 (2012).
- G. Kresse, J. Furthmüller, Efficient iterative schemes for ab initio total-energy calculations using a plane-wave basis set. Phys. Rev. B 54, 11169-11186 (1996).
- G. Kresse, D. Joubert, From ultrasoft pseudopotentials to the projector augmented-wave method Phys. Rev. B 59, 1758-1775 (1999).
- J. P. Perdew, Y. Wang, Accurate and simple analytic representation of the electron-gas correlation energy. Phys. Rev. B 45, 13244-13249 (1992).